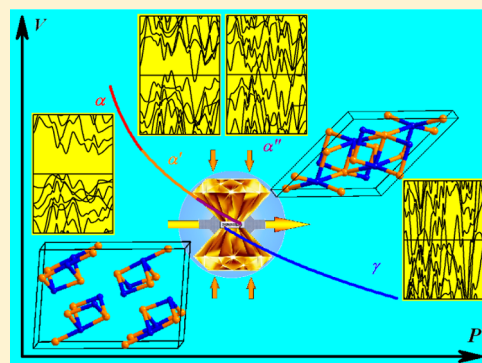


## Structural Phase Transitions and Metallized Phenomena in Arsenic Telluride under High Pressure

Jinggeng Zhao,<sup>\*,†</sup> Liuxiang Yang,<sup>§,||</sup> Zhenhai Yu,<sup>§</sup> Yong Wang,<sup>‡</sup> Chunyu Li,<sup>§</sup> Ke Yang,<sup>⊥</sup> Zhiguo Liu,<sup>\*,‡</sup> and Yi Wang<sup>\*,†</sup><sup>†</sup>Natural Science Research Center, Academy of Fundamental and Interdisciplinary Sciences, and <sup>‡</sup>Department of Physics, Harbin Institute of Technology, Harbin 150080, China<sup>§</sup>Center for High Pressure Science and Technology Advanced Research, Shanghai 201203, China<sup>||</sup>High Pressure Synergetic Consortium (HPSynC), Geophysical Laboratory, Carnegie Institution of Washington, Argonne, Illinois 60439, United States<sup>⊥</sup>Shanghai Institute of Applied Physics, Chinese Academy of Sciences, Shanghai 201203, China

## Supporting Information

**ABSTRACT:** In this study, first-principle calculations, *in situ* angle-dispersive X-ray diffraction, and *in situ* electrical resistance measurements were performed on arsenic telluride ( $\text{As}_2\text{Te}_3$ ) under high pressure. Structural phase transitions and metallized phenomena were observed from the calculated and experimental results. Upon compression,  $\alpha\text{-As}_2\text{Te}_3$  transforms into phases  $\alpha'$  and  $\alpha''$  at  $\sim 5.09$  and  $\sim 13.2$  GPa, respectively, with two isostructural phase transitions. From 13.2 GPa,  $\text{As}_2\text{Te}_3$  starts to transform into phase  $\gamma$ , with one first-order monoclinic to monoclinic crystal structural phase transition. According to the first-principle calculations and electrical resistance measurements, the structural phase transitions in the compression process induce the transformation from an insulator (phase  $\alpha$ ) across a semimetal (phase  $\alpha'$ ) into a metal (phases  $\alpha''$  and  $\gamma$ ). The evolution of the structure and transport property upon compression on  $\text{As}_2\text{Te}_3$  is helpful for understanding the properties of other  $\text{A}_2\text{B}_3$ -type compounds under high pressure.



## INTRODUCTION

Recently, in Cr-doped  $(\text{Bi}/\text{Sb})_2\text{Te}_3$  thin films, the quantum anomalous Hall (QAH) effect was observed,<sup>1</sup> which showed that topological insulators remain a hot topic in physical and material research. The related  $\text{A}_2\text{B}_3$ -type tellurides  $\text{Bi}_2\text{Te}_3$  and  $\text{Sb}_2\text{Te}_3$ , which are composed of the group V and VI elements, could be used as the simplest three-dimensional topological insulators.<sup>2</sup> Under ambient conditions, they adopt a layered rhombohedral structure (phase  $\alpha$ ) with a space group  $R\bar{3}m$ ,<sup>3</sup> in which the A and B layers stack alternately along the  $c$ -axis. Pressure plays an important role in modulating the structure and physical properties of these compounds.<sup>4,5</sup> The first-principle calculations and *in situ* high-pressure structural experiments showed that  $\text{Bi}_2\text{Te}_3$  and  $\text{Sb}_2\text{Te}_3$  transform into a seven-fold monoclinic structure (phase  $\beta$ ) and further into an eight-fold monoclinic structure (phase  $\gamma$ ), with space groups  $C2/m$  and  $C2/c$ , respectively.<sup>4</sup> At higher pressures, they crystallize into a disordered substitution alloy, with a body-centered cubic (BCC) structure (space group  $Im\bar{3}m$ ), according to the experimental results.<sup>4</sup> In the calculated works, an ordered nine- or ten-fold monoclinic structure (phase  $\delta$ , space group  $C2/m$ ) was set as an indication of this disordered BCC phase.<sup>4a,d</sup> On the other hand, the *ab initio* calculations and measured *in situ* high-pressure physical properties indicated that

$\text{Bi}_2\text{Te}_3$  and  $\text{Sb}_2\text{Te}_3$  transform into a topological superconductor upon compression, with an electronic topological transition (ETT) at the critical pressure, in which they still adopt the primal rhombohedral structure.<sup>5</sup> Up to the maximal experimental pressure, they maintain their superconductivity at low temperatures.<sup>5</sup> Therefore, the high-pressure works could provide significant information about the relationship between the crystal structure and physical property in the investigations of correlative materials.

Although possessing a chemical composition similar to those of  $\text{Bi}_2\text{Te}_3$  and  $\text{Sb}_2\text{Te}_3$ , the  $\text{A}_2\text{B}_3$ -type compound arsenic telluride ( $\text{As}_2\text{Te}_3$ ) adopts a six-fold monoclinic structure (phase  $\alpha$ , space group  $C2/m$ ) under ambient conditions.<sup>6</sup> The crystal structure of  $\alpha\text{-As}_2\text{Te}_3$  is different from that of  $\alpha\text{-Bi}_2\text{Te}_3$  and  $\alpha\text{-Sb}_2\text{Te}_3$ <sup>3</sup> and is also not the same as the high-pressure seven-fold monoclinic structure of  $\beta\text{-Bi}_2\text{Te}_3$  and  $\beta\text{-Sb}_2\text{Te}_3$ .<sup>4</sup> The earlier investigation of thermoelectric materials indicated that the thermoelectric coefficient (ZT) of  $\alpha\text{-As}_2\text{Te}_3$  is smaller than that of  $\alpha\text{-Bi}_2\text{Te}_3$ .<sup>7</sup> Under high-pressure and high-temperature conditions,  $\alpha\text{-As}_2\text{Te}_3$  transforms into a rhombohedral structure (phase  $\beta$ , space group  $R\bar{3}m$ ),<sup>8</sup> which is

Received: January 11, 2016

Published: April 1, 2016

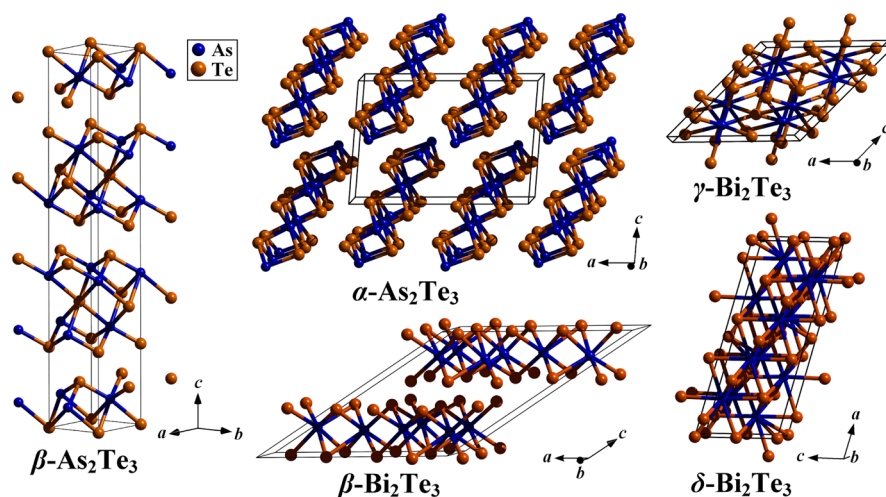


**Figure 1.** Schematic views of the possible crystal structures of  $\text{As}_2\text{Te}_3$  at high pressures, i.e.,  $\alpha\text{-As}_2\text{Te}_3$ ,  $\beta\text{-As}_2\text{Te}_3$ ,  $\beta\text{-Bi}_2\text{Te}_3$ ,  $\gamma\text{-Bi}_2\text{Te}_3$ , and  $\delta\text{-Bi}_2\text{Te}_3$  structure types. The blue and golden spheres represent the As and Te atoms, respectively. The black bold lines denote the unit cells.

isostructural to  $\alpha\text{-Bi}_2\text{Te}_3$  and  $\alpha\text{-Sb}_2\text{Te}_3$ .<sup>3</sup> This rhombohedral phase could also be obtained by quenching the melted  $\text{As}_2\text{Te}_3$  sample and displays good thermoelectric properties upon Sn doping with a peak ZT of 0.65 at 423 K.<sup>9</sup> Temperature could modulate the crystal structure of phase  $\beta$ . At 480 K, it irreversibly recovers to  $\alpha\text{-As}_2\text{Te}_3$  and transforms into a new  $\beta'$ - $\text{As}_2\text{Te}_3$  (space group  $P2_1/m$ ) at low temperatures.<sup>10</sup> A high-pressure work on the structure and thermoelectric properties showed that  $\alpha\text{-As}_2\text{Te}_3$  transforms into phase  $\beta$  at  $\sim 7$  GPa and room temperature, obtained from a common X-ray diffractometer in laboratory, which results in a dramatic enhancement in thermoelectric power.<sup>11</sup> According to the first-principle calculations, the uniaxial strain could cause an ETT from a band to a topological insulating state in  $\beta\text{-As}_2\text{Te}_3$ .<sup>12</sup> In light of the novel crystal structure and thermoelectric property, it is necessary to perform further high-pressure investigations with  $\text{As}_2\text{Te}_3$ , to explore the evolution of its structure and physical properties upon compression.

In this work, by performing first-principle calculations, we predicted the pressure-induced first-order monoclinic to monoclinic crystal structure phase transition in  $\text{As}_2\text{Te}_3$  from the enthalpy difference curves, which was then confirmed by the *in situ* angle-dispersive synchrotron X-ray diffraction (AD-XRD) experiments with a diamond anvil cell (DAC) technique. The experimental and calculated results showed that  $\text{As}_2\text{Te}_3$  undergoes two isostructural phase transitions (IPT) before transforming into the high-pressure phase mentioned above. The calculated electrical structures indicated that the crystal structure phase transitions induced the metallization in  $\text{As}_2\text{Te}_3$ , which was checked by *in situ* high-pressure electrical resistance measurements.

## EXPERIMENTAL AND COMPUTATIONAL SECTION

The structural relaxations and electronic calculations were conducted by using the first-principle density functional theory (DFT) with the Perdew–Burke–Ernzerhof generalized gradient approximation (PBE-GGA)<sup>13</sup> as implemented in the Vienna *ab initio* simulation package (VASP) code.<sup>14</sup> The interactions between electrons and ions were modeled by the projector-augmented wave (PAW) method.<sup>15</sup> The treated valence electrons were the  $4s^24p^3$  and  $5s^25p^4$  electrons for the As and Te atoms, respectively. The  $11 \times 11 \times 4$ ,  $11 \times 11 \times 11$ ,  $11 \times 11 \times 4$ ,  $9 \times 9 \times 6$ , and  $9 \times 9 \times 10$  Monkhorst–Pack  $k$ -point meshes were employed for the possible crystal structures of  $\text{As}_2\text{Te}_3$  under high

pressure, with  $\alpha\text{-As}_2\text{Te}_3$ ,  $\beta\text{-As}_2\text{Te}_3$ ,  $\beta\text{-Bi}_2\text{Te}_3$ ,  $\gamma\text{-Bi}_2\text{Te}_3$ , and  $\delta\text{-Bi}_2\text{Te}_3$  structure types, respectively. The plane-wave cutoff was set to be 300 eV, which could ensure that all the calculations of the total energy converged well within 1 meV/atom. The threshold for electronic self-consistency was equal to  $10^{-6}$  eV/cell. The break condition for all forces among ions in the ionic relaxation loop was smaller than 0.01 eV/Å.

The *in situ* high-pressure AD-XRD experiments on  $\text{As}_2\text{Te}_3$  were conducted at room temperature at beamline X17C of the National Synchrotron Light Source (NSLS, Brookhaven National Laboratory, Upton, NY) and beamline BL15U1 of the Shanghai Synchrotron Radiation Facility (SSRF), using a monochromatic X-ray beam with incident wavelengths of 0.4112 and 0.6199 Å, respectively. In the high-pressure experiments, the symmetric DACs maintain the rectangular slit in the emergent direction, with a diameter of 500 or 300  $\mu\text{m}$  of the flat culets in the diamonds. A T301 stainless steel gasket was preindented to a thickness of 40–55  $\mu\text{m}$  and then a 100–160  $\mu\text{m}$  diameter hole was drilled in the sample chamber. The  $\alpha\text{-As}_2\text{Te}_3$  sample, which was purchased from Alfa Aesar Co., was prepressed to a pellet with a thickness of approximately 10–15  $\mu\text{m}$  and then was loaded into the sample chamber. The ruby fluorescence method was used to measure the pressure.<sup>16</sup> Silicone oil was used as the pressure-transmitting medium, which could ensure a quasi-hydrostatic pressure environment.<sup>17</sup> Two-dimensional diffraction patterns were collected on a charge-coupled device (CCD) detector. The  $\text{CeO}_2$  standard was used to calibrate the distance between the sample and detector and the orientation parameters of the detector. The recorded images were integrated by using Fit2D program.<sup>18</sup> The high-pressure XRD patterns are refined by using the Rietveld methods<sup>19</sup> with the General Structure Analysis System (GSAS) program package.<sup>20</sup> The PowderCell program package was also used in analyzing the crystal structure.<sup>21</sup>

The high-pressure electrical resistance measurements for  $\text{As}_2\text{Te}_3$  were performed by using the standard four-electrode method in a DAC, in which the diameter of the flat culets in the diamonds was 300  $\mu\text{m}$ . A T301 stainless steel gasket was preindented to a thickness of 40  $\mu\text{m}$ , and the center of the gasket on the culet was removed by laser to form a hole. Fine cubic boron nitride (cBN) powder was used to cover the gasket as an insulating layer. cBN powder was pressed and further drilled into a center chamber of 100  $\mu\text{m}$  in diameter. The  $\alpha\text{-As}_2\text{Te}_3$  powder sample was loaded into this chamber without the pressure-transmitting medium. Slim gold wires with a diameter of 18  $\mu\text{m}$  were used as electrodes. The pressure in chamber was determined by the ruby fluorescence method.<sup>16</sup>

## RESULTS AND DISCUSSION

Considering its chemical composition is similar to those of  $\text{Bi}_2\text{Te}_3$  and  $\text{Sb}_2\text{Te}_3$ ,  $\text{As}_2\text{Te}_3$  may undergo similar structural

evolutions at high pressures. Therefore, the crystal structures of  $\text{Bi}_2\text{Te}_3$  and  $\text{Sb}_2\text{Te}_3$  upon compression could be selected as the possible high-pressure phases of  $\text{As}_2\text{Te}_3$ . Figure 1 shows the schematic views of possible crystal structures of  $\text{As}_2\text{Te}_3$  under high pressure, i.e.,  $\alpha\text{-As}_2\text{Te}_3$ ,  $\beta\text{-As}_2\text{Te}_3$ ,  $\beta\text{-Bi}_2\text{Te}_3$ ,  $\gamma\text{-Bi}_2\text{Te}_3$ , and  $\delta\text{-Bi}_2\text{Te}_3$  structure types. On the basis of these structures, the enthalpy difference curves (relative to  $\beta\text{-As}_2\text{Te}_3$ ) under high pressure are obtained, as shown in Figure 2. According to the

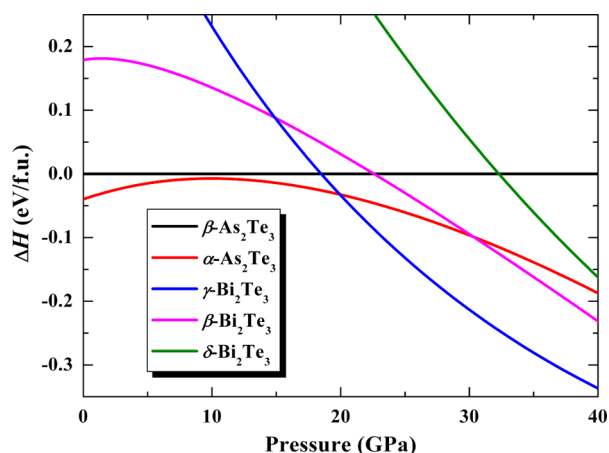


**Figure 2.** Enthalpy difference (relative to  $\beta\text{-As}_2\text{Te}_3$ ) vs pressure for the possible crystal structures of  $\text{As}_2\text{Te}_3$  upon compression, i.e.,  $\alpha\text{-As}_2\text{Te}_3$ ,  $\beta\text{-As}_2\text{Te}_3$ ,  $\beta\text{-Bi}_2\text{Te}_3$ ,  $\gamma\text{-Bi}_2\text{Te}_3$ , and  $\delta\text{-Bi}_2\text{Te}_3$  structure types.

calculated results, phase  $\alpha$  is the stable structure of  $\text{As}_2\text{Te}_3$  below  $\sim 20$  GPa and transforms into the  $\gamma\text{-Bi}_2\text{Te}_3$  structure type at 20 GPa, without intermediate  $\beta\text{-As}_2\text{Te}_3$  and  $\beta\text{-Bi}_2\text{Te}_3$  structure types. The calculated structural evolutions of  $\text{As}_2\text{Te}_3$  upon compression are confirmed by following *in situ* high-pressure AD-XRD experimental results. Because  $\beta\text{-As}_2\text{Te}_3$  has been obtained by high-pressure and high-temperature methods,<sup>8</sup> the new high-pressure structure of  $\text{As}_2\text{Te}_3$  in this work is denoted as phase  $\gamma$ , in which As and Te atoms form a three-dimensional netlike structure.

Figure 3 shows the selected XRD patterns of  $\text{As}_2\text{Te}_3$  up to 40.8 GPa at room temperature obtained at beamline X17C of NSLS with a wavelength of 0.4112 Å.  $\text{As}_2\text{Te}_3$  starts the transition from phase  $\alpha$  to  $\gamma$  at 13.2 GPa and transforms completely into phase  $\gamma$  at 26.5 GPa, without any evidence of the  $\beta\text{-As}_2\text{Te}_3$  and  $\beta\text{-Bi}_2\text{Te}_3$  structure types in the experimental pressure range, which is consistent with the calculated results mentioned above. In the XRD patterns, a weak peak exists at  $2\theta$  of  $\sim 10.0^\circ$ , indicated with an asterisk (\*), and another weak peak starts to emerge from 40.8 GPa at  $2\theta$  of  $\sim 9.6^\circ$ , indicated with a number sign (#). These two peaks do not belong to phase  $\alpha$  or  $\gamma$  of  $\text{As}_2\text{Te}_3$ . To understand them, another independent AD-XRD experiment up to 50.4 GPa at room temperature was performed at beamline BL15U1 of SSRF with a wavelength of 0.6199 Å. The selected XRD patterns are shown in Figure S1 of the Supporting Information. It is possible for  $\text{As}_2\text{Te}_3$  to decompose partly into a new compound (corresponding to the asterisk peak) upon compression, and then this new material transforms into another phase indicated by the number sign peak at higher pressures.

At high pressures and high temperatures,  $\alpha\text{-As}_2\text{Te}_3$  could transform into phase  $\beta$ .<sup>8</sup> Although other experimental results showed it also happens at  $\sim 7$  GPa and room temperature,<sup>11</sup> this phase transition could not be observed in our work under

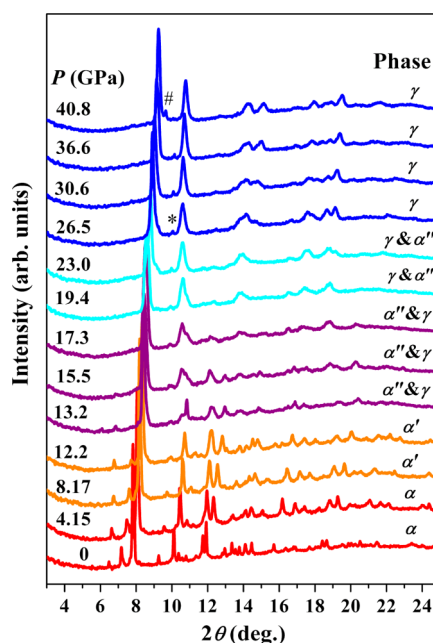


**Figure 3.** Selected angle-dispersive X-ray diffraction (AD-XRD) patterns of  $\text{As}_2\text{Te}_3$  at room temperature up to 40.8 GPa ( $\lambda = 0.4112$  Å).

the same conditions. As shown in Figure S2 of the Supporting Information, phases  $\alpha$  and  $\beta$  are similar to each other in their local structures, i.e., the  $[\text{As}_4\text{Te}_6]_n$  ribbon structure in the former and the  $\text{Te}(1)\text{-As-Te}(2)\text{-As-Te}(1)$  quintuple-layer structure in the latter. The coordination number (CN) of As or Te atoms in  $\text{As}_2\text{Te}_3$  is equal to 6 for phases  $\alpha$  and  $\beta$ . According to the enthalpy difference curves in Figure 2 and the similar local structures, phase  $\beta$  is a metastable structure of  $\text{As}_2\text{Te}_3$ .<sup>9,10</sup> High-pressure sintering could modulate  $\alpha\text{-As}_2\text{Te}_3$  into phase  $\beta$ , but it is not easy to achieve this transition by pressure only at room temperature. A similar case also exists in  $\text{A}_2\text{B}_3$ -type compound  $\text{Bi}_2\text{Se}_3$ ,<sup>22,23</sup> which is isostructural to  $\text{Bi}_2\text{Te}_3$  and  $\text{Sb}_2\text{Te}_3$  under ambient conditions and could be used as a topological insulator.<sup>2</sup> Via quenching under high-pressure and high-temperature conditions,  $\text{Bi}_2\text{Se}_3$  crystallizes into a metastable phase with an orthorhombic structure (space group  $Pnma$ ).<sup>22</sup> However,  $\text{Bi}_2\text{Se}_3$  could not transform into this orthorhombic structure at room temperature up to  $\sim 81$  GPa.<sup>23</sup>

By using the Le Bail refinement methods, the lattice parameters ( $a$ ,  $b$ ,  $c$ , and  $\beta$ ) and unit cell volume ( $V$ ) of  $\text{As}_2\text{Te}_3$  at each pressure are listed in Table S1 of the Supporting Information. Figure 4 shows the pressure dependences of  $a$ ,  $b$ ,  $c$ , and  $\beta$  of  $\alpha\text{-As}_2\text{Te}_3$ , in which the black bold lines are guides for the eyes. Because the  $[\text{As}_4\text{Te}_6]_n$  ribbon structure extends along the  $b$ -axis, Figure 4 also displays the  $a/b$  and  $c/b$  axial ratios. The calculated relationships of lattice parameters and axial ratios versus pressure are plotted in Figure 4, as well, and show the tendencies similar to those of the experimental results. With increasing pressure, lattice parameters  $a$ ,  $b$ , and  $c$  decrease when the pressure is  $< 13.2$  GPa, without any discontinuous change in the pressure range of 0–12.2 GPa. However, there is an inflection point at  $\sim 5.09$  GPa in the relationships of  $a/b$  and  $\beta$  angle versus pressure. Therefore, a pressure-induced IPT starts from  $\sim 5.09$  GPa, which indicates that  $\alpha\text{-As}_2\text{Te}_3$  transforms into phase  $\alpha'$ , keeping the space group unchanged. When the pressure is  $> 13.2$  GPa, the value of the  $a$ -axis increases and that of the  $b$ - and  $c$ -axes decreases with increasing pressure. The

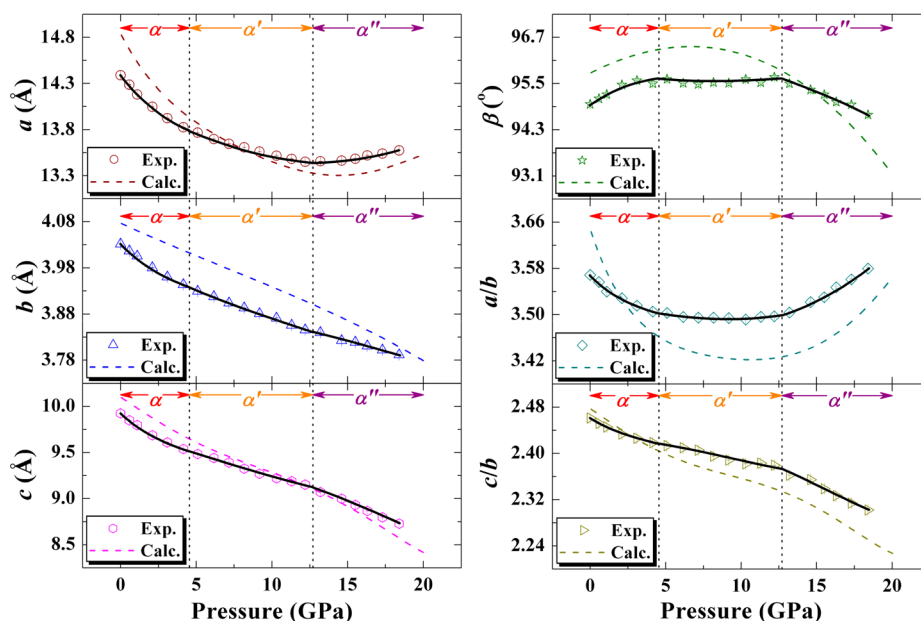


**Figure 4.** Pressure dependencies of lattice parameters ( $a$ ,  $b$ ,  $c$ , and  $\beta$ ) and axial ratios ( $a/b$  and  $c/b$ ) for  $\alpha$ - $\text{As}_2\text{Te}_3$  (including  $\alpha'$  and  $\alpha''$ ). The black bold lines are guides for the eyes. The whole pressure range is divided into three regions by the black vertical dotted lines according to the persistent ranges of phases  $\alpha$ ,  $\alpha'$ , and  $\alpha''$ .

relationships of  $\beta$  angle,  $a/b$ , and  $c/b$  versus pressure also exhibit inflection points at this pressure. Therefore, another IPT happens at  $\sim 13.2$  GPa, which shows that  $\alpha'$ - $\text{As}_2\text{Te}_3$  transforms into phase  $\alpha''$ , with the same space group as that of phases  $\alpha$  and  $\alpha'$ .

Figure 5 summarizes the relationship of volume per  $\text{As}_2\text{Te}_3$  chemical formula unit ( $V/\text{f.u.}$ ) for phases  $\alpha$  (including  $\alpha'$  and

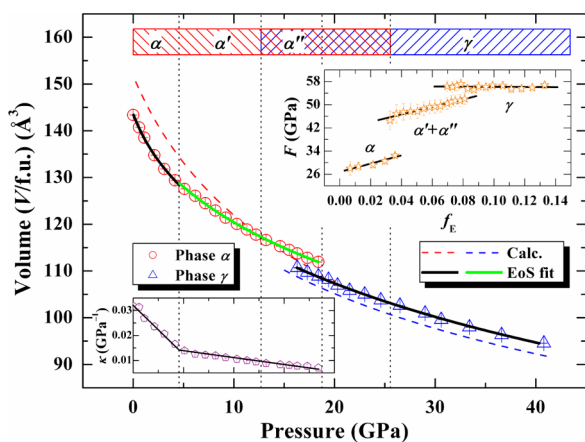


**Figure 5.** Pressure dependencies of volume per  $\text{As}_2\text{Te}_3$  chemical formula ( $V/\text{f.u.}$ ) for phases  $\alpha$  (including  $\alpha'$  and  $\alpha''$ ) and  $\gamma$ . The bold lines represent the fitting results to experimental data by using the Birch–Murnaghan equation of state (BM-EoS). The black vertical dotted lines at  $\sim 4.6$  and  $\sim 12.7$  GPa indicate the transition from phase  $\alpha$  to  $\alpha'$  and from phase  $\alpha'$  to  $\alpha''$ , respectively, and those at  $\sim 18.8$  and  $\sim 25.6$  GPa indicate that phase  $\gamma$  turns into the main structure of  $\text{As}_2\text{Te}_3$  and phase  $\alpha''$  transforms completely into phase  $\gamma$ , respectively. The inset in the bottom left corner shows the relationship of volume compressibility ( $\kappa$ ) vs pressure for phases  $\alpha$ ,  $\alpha'$ , and  $\alpha''$ , with the same horizontal axis as the master figure, in which the black bold lines are guides for the eyes. The inset in the top right corner shows the normalized pressure vs Eulerian strain ( $f_E$ – $F$ ) plots, in which the black bold lines represent the linear fits to the  $f_E$ – $F$  data.

$\alpha''$ ) and  $\gamma$  at 0–40.8 GPa. There are two main regions in Figure 5, corresponding to phases  $\alpha$  (including  $\alpha'$  and  $\alpha''$ ) and  $\gamma$  under high pressures, and the pressure range of 13.2–23.0 GPa represents the region of coexistence of phases  $\alpha''$  and  $\gamma$ . The calculated  $V$ – $P$  relationships are also plotted in Figure 5, which show tendencies similar to those of the experimental results. With increasing pressure, the volume decreases for these phases of  $\text{As}_2\text{Te}_3$ , with a 2.6% collapse for the transition from phase  $\alpha''$  to  $\gamma$ . The solid lines represent the fitting results for the  $V$ – $P$  relationships of  $\text{As}_2\text{Te}_3$  by using the Birch–Murnaghan equation of state (BM-EoS).<sup>24</sup> The pressure dependence of volume compressibility [ $\kappa = -(\partial V/\partial P)/V$ ] for phases  $\alpha$ ,  $\alpha'$ , and  $\alpha''$  is shown in the bottom left corner of Figure 5, and linear fitting of the five adjacent data yields the slope ( $\partial V/\partial P$ ) of the center point, in which the black bold lines are guides for the eyes. Although no discontinuous change exists in the  $V$ – $P$  curve at the transition from phase  $\alpha$  to  $\alpha'$ , the  $\kappa$ – $P$  relationship shows a turning point at this critical pressure, so it is difficult to fit the  $V$ – $P$  curves of phases  $\alpha$  and  $\alpha'$  together by using one function. The ambient-pressure isothermal bulk modulus  $B_0$  is estimated to be 26(2), 42(4), and 56(1) GPa for phases  $\alpha$ ,  $\alpha' + \alpha''$ , and  $\gamma$ , respectively, with first-order pressure derivative  $B_0'$  values of 9.0(1.6), 6.1(1), and 4, respectively. The fitted ambient unit cell volume ( $V_0/\text{f.u.}$ ) is equal to 143.6(2), 140.3(8), and 134.6(6)  $\text{\AA}^3$  for phases  $\alpha$ ,  $\alpha' + \alpha''$ , and  $\gamma$ , respectively. With  $B_0'$  set to 4,  $B_0$  is equal to 33(1) and 59.3(8) GPa for phases  $\alpha$  and  $\alpha' + \alpha''$ , respectively. The  $f_E$ – $F$  plots are shown in the inset in the top right corner of Figure 5, in which  $f_E$  and  $F$  denote Eulerian strain and normalized pressure, respectively.<sup>25</sup> The linear fit to the  $f_E$ – $F$  plots gives  $B_0$  values of 26.8(6), 41.5(5), and 56.4(8) GPa for phases  $\alpha$ ,  $\alpha' + \alpha''$ , and  $\gamma$ , respectively, with  $B_0'$  values of 7.5(1.4), 6.1(5), and 4, respectively, which are consistent with those obtained from the BM-EoS fit within the error range.

The XRD patterns of  $\text{As}_2\text{Te}_3$  below 12.2 GPa and above 26.5 GPa are refined by using the Rietveld methods. The typical experimental (empty circles) and fitted (lines) results of phases

$\alpha$  and  $\gamma$  at 4.15 and 30.6 GPa are shown in Figure 6, with  $R_{wp}$  factors of 3.14% and 1.85%, respectively. From the refinement

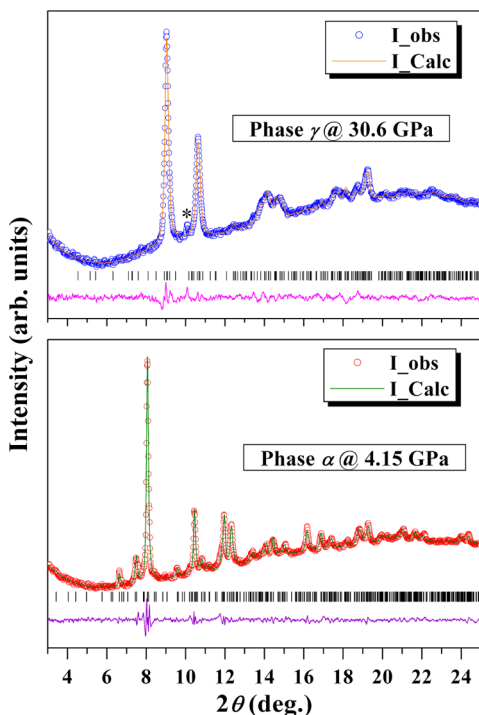


**Figure 6.** Experimental (empty circles) and fitted (lines) X-ray diffraction (XRD) patterns for phases  $\alpha$  and  $\gamma$  of  $\text{As}_2\text{Te}_3$  at 4.15 and 30.6 GPa ( $\lambda = 0.4112 \text{ \AA}$ ). The vertical lines denote the theoretical positions of the Bragg peaks. The difference curves between observed and calculated XRD patterns are shown at the bottom.

results in Figure 6, the lattice parameters and atomic coordinates of these two phases are listed in Table 1. The

**Table 1. Experimental Lattice Parameters and Atomic Coordinates of  $\alpha$ - and  $\gamma$ - $\text{As}_2\text{Te}_3$**

atom	site	x	y	z
Phase $\alpha$ @ 4.15 GPa				
Space Group $C2/m$ ; $a = 13.8243(15) \text{ \AA}$ , $b = 3.9439(3) \text{ \AA}$ , $c = 9.5378(12) \text{ \AA}$ , $\beta = 95.50(1)^\circ$ ; $R_p = 1.52\%$ , $R_{wp} = 3.14\%$				
As(1)	4i	0.1993(6)	0	0.1554(9)
As(2)	4i	0.0987(5)	0.5	0.4492(7)
Te(1)	4i	0.0292(3)	0	0.2850(5)
Te(2)	4i	0.2777(3)	0.5	0.3518(7)
Te(3)	4i	0.3673(3)	0	0.0368(5)
Phase $\gamma$ @ 30.6 GPa				
Space Group $C2/c$ ; $a = 9.252(3) \text{ \AA}$ , $b = 6.4825(11) \text{ \AA}$ , $c = 9.506(2) \text{ \AA}$ , $\beta = 135.69(1)^\circ$ ; $R_p = 1.16\%$ , $R_{wp} = 1.85\%$				
As	8f	0.2921(14)	0.1442(10)	0.8463(10)
Te(1)	8f	0.5706(8)	0.3862(7)	0.9367(6)
Te(2)	4e	0.5	-0.0899(10)	0.75

calculated lattice parameters and atomic coordinates of  $\alpha$ - and  $\gamma$ - $\text{As}_2\text{Te}_3$  at 4.5 and 29 GPa are also listed in Table 2. The pressure dependencies of atom mean distances for phases  $\alpha$  and  $\alpha'$  of  $\text{As}_2\text{Te}_3$  below 12.2 GPa are plotted in Figure 7, in which the As–Te(I) and As–Te(O) distances represent the average interval of As and Te atoms in one  $[\text{As}_4\text{Te}_6]_n$  ribbon and between two neighboring  $[\text{As}_4\text{Te}_6]_n$  ribbons, respectively, and the Te–Te distance represents the average interval of two Te

**Table 2. Calculated Lattice Parameters and Atomic Coordinates of  $\alpha$ - and  $\gamma$ - $\text{As}_2\text{Te}_3$**

atom	site	x	y	z
Phase $\alpha$ @ 4.5 GPa				
Space Group $C2/m$ ; $a = 13.9348 \text{ \AA}$ , $b = 4.0245 \text{ \AA}$ , $c = 9.6587 \text{ \AA}$ , $\beta = 96.367^\circ$				
As(1)	4i	0.1989	0	0.1414
As(2)	4i	0.6117	0	0.4499
Te(1)	4i	0.0246	0	0.2833
Te(2)	4i	0.7820	0	0.3423
Te(3)	4i	0.3795	0	0.0410
Phase $\gamma$ @ 29 GPa				
Space Group $C2/c$ ; $a = 9.2084 \text{ \AA}$ , $b = 6.4532 \text{ \AA}$ , $c = 9.5562 \text{ \AA}$ , $\beta = 136.161^\circ$				
As	8f	0.8021	0.1065	0.3549
Te(1)	8f	0.0911	0.3659	0.4569
Te(2)	4e	0	0.1411	0.75

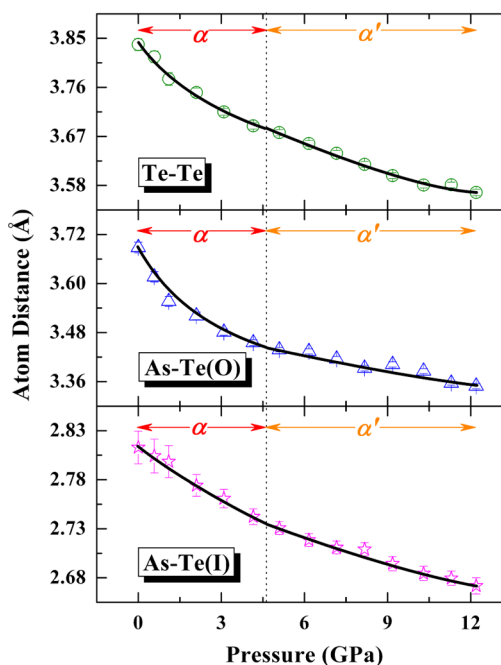


**Figure 7.** Pressure dependencies of atom mean distances for phases  $\alpha$  and  $\alpha'$  of  $\text{As}_2\text{Te}_3$  below 12.2 GPa. The black bold lines are guides for the eyes.

atoms between two neighboring  $[\text{As}_4\text{Te}_6]_n$  ribbons. All these distances decrease upon compression, with an inflection point at  $\sim 5.09$  GPa, which confirms the IPT from phase  $\alpha$  to  $\alpha'$ . In the pressure range of 0–12.2 GPa, the atom mean distance between two neighboring  $[\text{As}_4\text{Te}_6]_n$  ribbons [i.e., As–Te(O) and Te–Te distances] is larger than that in one  $[\text{As}_4\text{Te}_6]_n$  ribbon [i.e., As–Te(I) distance]. At high pressure, the shrinkage of the former is larger than that of the latter.

In the IPT, the space group and atom arrangement are the same as those before the phase transition. According to the evolution of lattice parameters and unit cell volume upon compression, there are three main types of IPT at high pressures. First, the volume collapses when the phase transition occurs, which indicates that the pressure-induced IPT belongs to the first-order phase transition, e.g., in cubic Ce, SmS, and  $\text{PbCrO}_3$ .<sup>26</sup> Second, the lattice parameters and volumes decrease continuously with increasing pressure in the structural evolution process, but the axial ratios behave a kink at the transition pressure, e.g., in the  $\text{A}_2\text{B}_3$ -type topological insulators

and related materials.<sup>27</sup> Third, one lattice parameter starts to increase from the transition pressure and decreases after the transformation, which behaves as a special and complex structural evolution process, e.g., in the iron-based superconductors and related parent compounds.<sup>28</sup> For  $\alpha$ -As<sub>2</sub>Te<sub>3</sub>, the transition from phase  $\alpha$  to  $\alpha'$  belongs to the second type of IPT and that from phase  $\alpha'$  to  $\alpha''$  behaves like the third one. Therefore,  $\alpha$ -As<sub>2</sub>Te<sub>3</sub> undergoes two different types of IPT upon compression. The two pressure-induced IPTs and the following first-order phase transition in As<sub>2</sub>Te<sub>3</sub> are similar to the structural evolutions upon compression in its sister compound As<sub>2</sub>O<sub>3</sub>.<sup>29</sup> However, it is difficult to obtain more information about the structural evolution process of  $\alpha''$ -As<sub>2</sub>Te<sub>3</sub> at higher pressures, because it coexists with phase  $\gamma$  when the second IPT happens. The *in situ* high-pressure single-crystal XRD experiments may provide more messages about the IPT in As<sub>2</sub>Te<sub>3</sub> upon compression, like that in As<sub>2</sub>O<sub>3</sub>.<sup>29</sup>

Generally, the lattice phase transitions are related to the electronic structure changes,<sup>30</sup> so the following theoretical calculations are performed for As<sub>2</sub>Te<sub>3</sub> based on the structure optimization. Figure 8 summarizes the energy bands and DOS

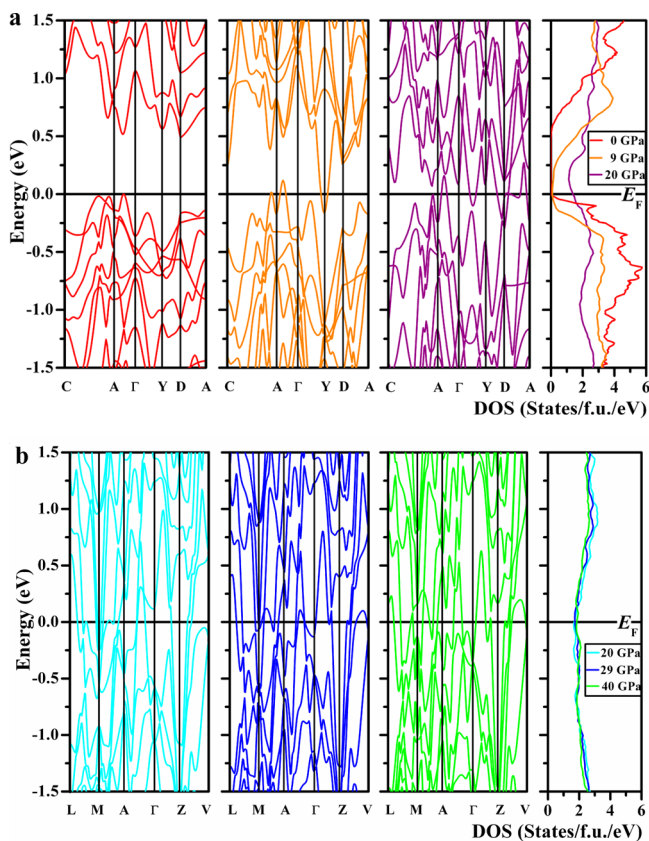


**Figure 8.** Calculated energy bands and total density of states (DOS) around the Fermi energy ( $E_F$ ) for phases (a)  $\alpha$  (including  $\alpha'$  and  $\alpha''$ ) and (b)  $\gamma$  of As<sub>2</sub>Te<sub>3</sub> at different pressures.

around the Fermi energy ( $E_F$ ) for phase  $\alpha$  (including  $\alpha'$  and  $\alpha''$ ) and  $\gamma$  of As<sub>2</sub>Te<sub>3</sub> at different pressures, which could reveal the evolution of the transport property upon compression. The band structures are calculated along the C–A– $\Gamma$ –Y–D–A and L–M–A– $\Gamma$ –Z–V paths in the  $k$ -space for phases  $\alpha$  and  $\gamma$ , respectively. For phases  $\alpha$  (including  $\alpha'$  and  $\alpha''$ ), the coordinates of points C and D are (–0.01337, 0.48380, 0.47715) and (0.47042, 0.47042, 0.45430), respectively.

According to the band structures,  $\alpha$ -As<sub>2</sub>Te<sub>3</sub> is an insulator at ambient pressure, with a band gap width ( $E_g$ ) of 0.47 eV. With increasing pressure,  $E_g$  decreases monotonously and reaches zero at  $\sim$ 5.4 GPa. When the pressure is  $>$ 5.4 GPa, As<sub>2</sub>Te<sub>3</sub> transforms into phase  $\alpha'$ . According to the energy bands in Figure 8a, the overlap of the valence band top and conduction band bottom indicates that phase  $\alpha'$  is a semimetal. When phase  $\alpha''$  comes into being, the metallicity of As<sub>2</sub>Te<sub>3</sub> is stronger than that of phase  $\alpha'$ . In the whole compression range of phases  $\alpha$ ,  $\alpha'$ , and  $\alpha''$ , the DOS at  $E_F$  increases with increasing pressure, which also shows the enhanced metallicity in the compression process.  $\gamma$ -As<sub>2</sub>Te<sub>3</sub> exhibits the obvious metallicity obtained from the energy bands and DOS in Figure 8b. The electronic structures mentioned above indicate that the insulating phase  $\alpha$  transforms across a semimetallic phase  $\alpha'$  into metallic phases  $\alpha''$  and  $\gamma$ , when loading pressure on As<sub>2</sub>Te<sub>3</sub>.

To check the calculated results on the transport properties of As<sub>2</sub>Te<sub>3</sub>, the *in situ* high-pressure electrical resistance measurements were performed in the pressure range of 2.65–39.1 GPa. Figure 9 shows the relationship of logarithm resistance versus

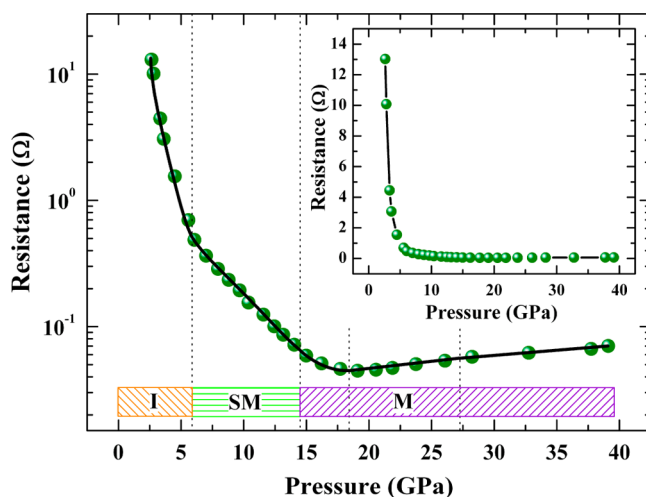


**Figure 9.** Pressure dependence of logarithm resistance of As<sub>2</sub>Te<sub>3</sub>. The black bold lines are guides for the eyes. I, SM, and M represent the insulator, semimetal, and metal, respectively. The inset shows the relationship of resistance vs pressure.

pressure for As<sub>2</sub>Te<sub>3</sub>, in which the black bold lines are guides for the eyes and I, SM, and M represent the insulator, semimetal, and metal, respectively. The pressure dependence of electrical resistance is plotted in the inset of Figure 9, as well. The electrical resistance drops sharply below  $\sim$ 5.59 GPa, and then the logarithm resistance exhibits an inflection point from  $\sim$ 6.07 GPa, which shows the transition from the insulator to semimetal according to the calculated results mentioned above. When the pressure is  $>$ 14.9 GPa, the logarithm resistance exhibits another inflection point, which is related to the transition from phase  $\alpha'$  to  $\alpha''$ , and As<sub>2</sub>Te<sub>3</sub> becomes a metal from this pressure. At pressures above 19.1 GPa, phase  $\gamma$  turns into the main structure of As<sub>2</sub>Te<sub>3</sub> according to the XRD patterns in Figure 3, which corresponds to a slight increase in electrical resistance with pressure. From  $\sim$ 28.2 GPa, the increment of electrical resistance with pressure changes to 1.1(1) m $\Omega$ /GPa from the value of 1.45(9) m $\Omega$ /GPa below 28.2 GPa. At this pressure, As<sub>2</sub>Te<sub>3</sub> transforms completely into phase  $\gamma$ . Therefore, the pressure dependence of electrical resistance is in good agreement with the results of the crystal

structure and electronic structure evolution upon compression in  $\text{As}_2\text{Te}_3$ .

For the  $\text{A}_2\text{B}_3$ -type tellurides  $\text{Bi}_2\text{Te}_3$ ,  $\text{Sb}_2\text{Te}_3$ , and  $\text{As}_2\text{Te}_3$ , the structure and physical properties at high pressure are related to the A-site atoms. Figure 10 summarizes the evolution of their

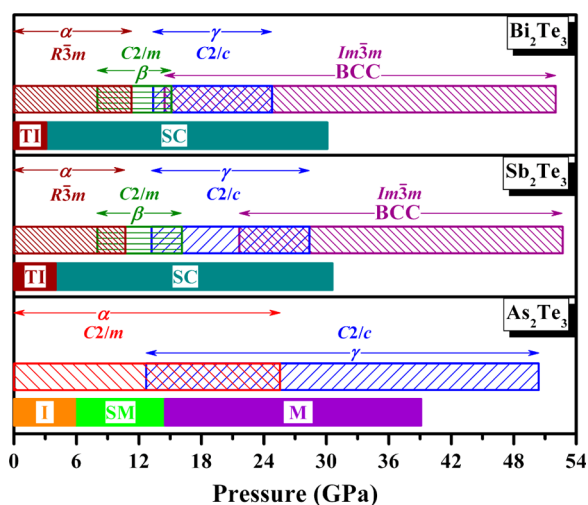


**Figure 10.** Phase diagrams of the evolution of the structure and transport property upon compression for  $\text{A}_2\text{B}_3$ -type tellurides  $\text{Bi}_2\text{Te}_3$ ,<sup>4,5</sup>  $\text{Sb}_2\text{Te}_3$ ,<sup>4,5</sup> and  $\text{As}_2\text{Te}_3$  (this work). The right edge of bars indicates the maximal pressure in the experiments. TI, SC, I, SM, and M represent the topological insulator, superconductor, insulator, semimetal, and metal, respectively.

structure and transport property upon compression,<sup>4,5</sup> in which TI, SC, I, SM, and M represent the topological insulator, superconductor, insulator, semimetal, and metal, respectively. Although adopting the different crystal structures under ambient conditions from  $\text{Bi}_2\text{Te}_3$  and  $\text{Sb}_2\text{Te}_3$ ,  $\text{As}_2\text{Te}_3$  could also transform into the same eight-fold monoclinic structure at high pressures. For phase  $\gamma$  of these binary tellurides, the unit cell volume decreases with a decreasing radius of A-site atoms (i.e., from Bi to As atoms).<sup>31</sup> Compared with  $\gamma\text{-Bi}_2\text{Te}_3$  and  $\gamma\text{-Sb}_2\text{Te}_3$ ,  $\gamma\text{-As}_2\text{Te}_3$  exists over a large pressure range.  $\text{Bi}_2\text{Te}_3$  and  $\text{Sb}_2\text{Te}_3$  adopt the disordered BCC structure at  $\sim 14.4$  and  $\sim 21.6$  GPa, respectively,<sup>4</sup> but  $\text{As}_2\text{Te}_3$  keeps the ordered monoclinic structure up to 50.4 GPa according to the results presented in this work. The different compression behavior between  $\text{As}_2\text{Te}_3$  and  $\text{Bi}_2\text{Te}_3/\text{Sb}_2\text{Te}_3$  may be due to the radius of the As atom being smaller than those of the Bi and Sb atoms.<sup>31</sup> The As, Sb, Bi, Te, and Se substances could transform into a BCC structure upon compression, with transition pressures of 97, 28, 7.7, 27, and 140 GPa, respectively.<sup>32</sup> The high transition pressure in the As substance is a possible reason for the difficulty of  $\text{As}_2\text{Te}_3$  crystallizing into this disordered BCC structure upon compression. A similar case could also be observed in  $\text{Bi}_2\text{Se}_3$ , which does not adopt this disordered BCC structure up to  $\sim 81$  GPa.<sup>23</sup> At higher pressures,  $\text{As}_2\text{Te}_3$  may transform into other phases, which needs to be tested by further high-pressure experiments. Upon compression,  $\text{Bi}_2\text{Te}_3$  and  $\text{Sb}_2\text{Te}_3$  could transform into a superconductor from the original topological insulator,<sup>5</sup> with an ETT at the critical pressure. According to this work, the crystal  $\text{As}_2\text{Te}_3$  transforms into a semimetal from an insulator at high pressures and then becomes a metal. It should be mentioned that the amorphous  $\text{As}_2\text{Te}_3$  could exhibit superconductivity at  $\sim 10$  GPa,<sup>33</sup> with a superconducting transition temperature ( $T_c$ ) of  $\sim 4.4$  K, which is close to that

of  $\text{Bi}_2\text{Te}_3$  and  $\text{Sb}_2\text{Te}_3$ .<sup>5</sup> Taking into account these issues, we conclude that further *in situ* high-pressure investigations of physical properties at low temperatures could explore whether  $\text{As}_2\text{Te}_3$  will transform into a superconductor upon compression.

## CONCLUSIONS

In conclusion, two isostructural phase transitions and one first-order crystal structural phase transition in  $\text{As}_2\text{Te}_3$  at high pressure were discovered at room temperature by the first-principle calculations and *in situ* high-pressure angle-dispersive X-ray diffraction experiments, in which  $\text{As}_2\text{Te}_3$  adopts a monoclinic structure in the experimental pressure range. The modulations of the crystal lattice during structural evolution indicate that  $\text{As}_2\text{Te}_3$  transforms into a semimetal from the original insulator and becomes a metal at higher pressures, which is obtained from the *ab initio* calculations and *in situ* high-pressure electrical resistance measurements. These pressure-induced crystal structure and transport property transitions will improve our understanding of the universal structure evolution and physical property patterns for these  $\text{A}_2\text{B}_3$ -type tellurides at ambient and high pressures.

## ASSOCIATED CONTENT

### Supporting Information

The Supporting Information is available free of charge on the ACS Publications website at DOI: 10.1021/acs.inorgchem.6b00073.

All the lattice parameters and unit cell volumes of  $\text{As}_2\text{Te}_3$  (Table S1), selected high-pressure XRD patterns of  $\text{As}_2\text{Te}_3$  (Figure S1), and schematic views of the local structures in  $\alpha$ - and  $\beta$ - $\text{As}_2\text{Te}_3$  (Figure S2) (PDF)

## AUTHOR INFORMATION

### Corresponding Authors

\*Phone: +86/451/86418430. E-mail: zhaojingeng@163.com.

\*E-mail: liuzhiguo@hit.edu.cn.

\*E-mail: yw@hit.edu.cn.

### Notes

The authors declare no competing financial interest.

## ACKNOWLEDGMENTS

We are grateful for the support from the National Natural Science Foundation of China (Grants 11274081, 10904022, and 10904024), the Postdoctoral Science-research Developmental Foundation of Heilongjiang Province (Grant LBH-Q12095), and the Fundamental Research Funds for the Central Universities (Grant HIT.NSRIF.2013054). We thank the High Performance Computing Center of the Harbin Institute of Technology for calculation resources. Use of NSLS is supported by the U.S. Department of Energy (DOE), Office of Science, Office of Basic Energy Sciences, under Contract DE-AC02-98CH10886. Beamline X17 of NSLS is supported by the Consortium for Materials Properties Research in Earth Sciences (COMPRES). Parts of this work were performed at beamline BL15U1 of SSRF. We are also grateful to Dr. Zhiqiang Chen and Dr. Xinguo Hong (NSLS) for X-ray diffraction measurements.

## REFERENCES

- (1) Chang, C. Z.; Zhang, J. S.; Feng, X.; Shen, J.; Zhang, Z. C.; Guo, M. H.; Li, K.; Ou, Y. B.; Wei, P.; Wang, L.-L.; Ji, Z.-Q.; Feng, Y.; Ji, S.

- H.; Chen, X.; Jia, J. F.; Dai, X.; Fang, Z.; Zhang, S.-C.; He, K.; Wang, Y. U.; Lu, L.; Ma, X. C.; Xue, Q. K. *Science* **2013**, *340*, 167–170.
- (2) (a) Zhang, H.; Liu, C. X.; Qi, X. L.; Dai, X.; Fang, Z.; Zhang, S. C. *Nat. Phys.* **2009**, *5*, 438–442. (b) Chen, Y. L.; Analytis, J. G.; Chu, J.-H.; Liu, Z. K.; Mo, S.-K.; Qi, X. L.; Zhang, H. J.; Lu, D. H.; Dai, X.; Fang, Z.; Zhang, S. C.; Fisher, I. R.; Hussain, Z.; Shen, Z.-X. *Science* **2009**, *325*, 178–181.
- (3) (a) Nakajima, S. *J. Phys. Chem. Solids* **1963**, *24*, 479–485. (b) Anderson, T. L.; Krause, H. B. *Acta Crystallogr., Sect. B: Struct. Crystallogr. Cryst. Chem.* **1974**, *30*, 1307–1310.
- (4) (a) Zhu, L.; Wang, H.; Wang, Y. C.; Lv, J.; Ma, Y. M.; Cui, Q. L.; Ma, Y. M.; Zou, G. T. *Phys. Rev. Lett.* **2011**, *106*, 145501. (b) Einaga, M.; Ohmura, A.; Nakayama, A.; Ishikawa, F.; Yamada, Y.; Nakano, S. *Phys. Rev. B: Condens. Matter Mater. Phys.* **2011**, *83*, 092102. (c) Zhao, J. G.; Liu, H. Z.; Ehm, L.; Chen, Z. Q.; Sinogeikin, S.; Zhao, Y. S.; Gu, G. D. *Inorg. Chem.* **2011**, *50*, 11291–11293. (d) Ma, Y. M.; Liu, G. T.; Zhu, P. W.; Wang, H.; Wang, X.; Cui, Q. L.; Liu, J.; Ma, Y. M. *J. Phys.: Condens. Matter* **2012**, *24*, 475403.
- (5) (a) Zhang, C.; Sun, L. L.; Chen, Z. Y.; Zhou, X. J.; Wu, Q.; Yi, W.; Guo, J.; Dong, X. L.; Zhao, Z. X. *Phys. Rev. B: Condens. Matter Mater. Phys.* **2011**, *83*, 140504. (b) Zhang, J. L.; Zhang, S. J.; Weng, H. M.; Zhang, W.; Yang, L. X.; Liu, Q. Q.; Feng, S. M.; Wang, X. C.; Yu, R. C.; Cao, L. Z.; Wang, L.; Yang, W. G.; Liu, H. Z.; Zhao, W. Y.; Zhang, S. C.; Dai, X.; Fang, Z.; Jin, C. Q. *Proc. Natl. Acad. Sci. U. S. A.* **2011**, *108*, 24–28. (c) Einaga, M.; Tanabe, Y.; Nakayama, A.; Ohmura, A.; Ishikawa, F.; Yamada, Y. *J. Phys.: Conf. Ser.* **2010**, *215*, 012036. (d) Zhu, J.; Zhang, J. L.; Kong, P. P.; Zhang, S. J.; Yu, X. H.; Zhu, J. L.; Liu, Q. Q.; Li, X.; Yu, R. C.; Ahuja, R.; Yang, W. G.; Shen, G. Y.; Mao, H. K.; Weng, H. M.; Dai, X.; Fang, Z.; Zhao, Y. S.; Jin, C. Q. *Sci. Rep.* **2013**, *3*, 2016.
- (6) Carron, G. *Acta Crystallogr.* **1963**, *16*, 338–343.
- (7) (a) Harman, T. C.; Paris, B.; Miller, S. E.; Goering, H. L. *J. Phys. Chem. Solids* **1957**, *2*, 181–190. (b) Black, J.; Conwell, E. M.; Seigle, L.; Spencer, C. W. *J. Phys. Chem. Solids* **1957**, *2*, 240–251.
- (8) Kirkinskii, V. A.; Yakushev, V. G. *Inorg. Mater.* **1974**, *10*, 1230–1233.
- (9) (a) Shu, H. W.; Jaulmes, S.; Flahaut, J. *J. Solid State Chem.* **1988**, *74*, 277–286. (b) Vaney, J. B.; Carreaud, J.; Delaizir, G.; Pradel, A.; Piarristeguy, A.; Morin, C.; Alleno, E.; Monnier, J.; Goncalves, A. P.; Candolfi, C.; Dauscher, A.; Lenoir, B. *Adv. Electron. Mater.* **2015**, *1*, 1400008.
- (10) (a) Toscani, S.; Dugué, J.; Ollitrault, R.; Céolin, R. *Thermochim. Acta* **1991**, *186*, 247–251. (b) Morin, C.; Corallini, S.; Carreaud, J.; Vaney, J. B.; Delaizir, G.; Crivello, J. C.; Lopes, E. B.; Piarristeguy, A.; Monnier, J.; Candolfi, C.; Nassif, V.; Cuello, G. J.; Pradel, A.; Goncalves, A. P.; Lenoir, B.; Alleno, E. *Inorg. Chem.* **2015**, *54*, 9936–9947.
- (11) Scheidemantel, T. J.; Meng, J. F.; Badding, J. V. *J. Phys. Chem. Solids* **2005**, *66*, 1744–1747.
- (12) Pal, K.; Waghmare, U. V. *Appl. Phys. Lett.* **2014**, *105*, 062105.
- (13) Perdew, J. P.; Burke, K.; Ernzerhof, M. *Phys. Rev. Lett.* **1996**, *77*, 3865–3868.
- (14) Kresse, G.; Furthmüller, J. *Phys. Rev. B: Condens. Matter Mater. Phys.* **1996**, *54*, 11169–11186.
- (15) Blöchl, P. E. *Phys. Rev. B: Condens. Matter Mater. Phys.* **1994**, *50*, 17953–17979.
- (16) Mao, H. K.; Xu, J. A.; Bell, P. M. *J. Geophys. Res.* **1986**, *91*, 4673–4676.
- (17) (a) Shen, Y. R.; Kumar, R. S.; Pravica, M.; Nicol, M. F. *Rev. Sci. Instrum.* **2004**, *75*, 4450–4454. (b) You, S. J.; Chen, L. C.; Jin, C. Q. *Chin. Phys. Lett.* **2009**, *26*, 096202. (c) Klotz, S.; Chervin, J.-C.; Munsch, P.; Le Marchand, G. *J. Phys. D: Appl. Phys.* **2009**, *42*, 075413.
- (18) Hammersley, A. P.; Svensson, S. O.; Hanfland, M.; Fitch, A. N.; Häusermann, D. *High Pressure Res.* **1996**, *14*, 235–248.
- (19) (a) Rietveld, H. M. *Acta Crystallogr.* **1967**, *22*, 151–152. (b) Rietveld, H. M. *J. Appl. Crystallogr.* **1969**, *2*, 65–71.
- (20) (a) Larson, A. C.; Von Dreele, R. B. *General Structure Analysis System (GSAS)*; Los Alamos National Laboratory, Report LAUR 86-748; Los Alamos National Laboratory: Los Alamos, NM, 1994.
- (b) Toby, B. H. *J. Appl. Crystallogr.* **2001**, *34*, 210–213.
- (21) Kraus, W.; Nolze, G. *J. Appl. Crystallogr.* **1996**, *29*, 301–303.
- (22) (a) Atabaeva, E. Ya.; Bendeliani, N. A.; Popova, S. V. *Sov. Phys. Solid State* **1973**, *15*, 2346–2348. (b) Atabaeva, E. Ya.; Mashkov, S. A.; Popova, S. V. *Sov. Phys. Crystallogr.* **1973**, *18*, 104–105.
- (23) (a) Zhao, J. G.; Liu, H. Z.; Ehm, L.; Dong, D. W.; Chen, Z. Q.; Gu, G. D. *J. Phys.: Condens. Matter* **2013**, *25*, 125602. (b) Liu, G. T.; Zhu, L.; Ma, Y. M.; Lin, C. L.; Liu, J.; Ma, Y. M. *J. Phys. Chem. C* **2013**, *117*, 10045–10050. (c) Kirshenbaum, K.; Syers, P. S.; Hope, A. P.; Butch, N. P.; Jeffries, J. R.; Weir, S. T.; Hamlin, J. J.; Maple, M. B.; Vohra, Y. K.; Paglione, J. *Phys. Rev. Lett.* **2013**, *111*, 087001. (d) Yu, Z. H.; Wang, L.; Hu, Q. Y.; Zhao, J. G.; Yan, S.; Yang, K.; Sinogeikin, S.; Gu, G. D.; Mao, H.-K. *Sci. Rep.* **2015**, *5*, 15939.
- (24) Birch, F. *Phys. Rev.* **1947**, *71*, 809–824.
- (25) (a) Angel, R. J. *Rev. Mineral. Geochem.* **2000**, *41*, 35–59. (b) Angel, R. J.; Gonzalez-Platas, J.; Alvaro, M. Z. *Kristallogr. - Cryst. Mater.* **2014**, *229*, 405–419.
- (26) (a) Lawrence, J. M.; Riseborough, P. S.; Parks, R. D. *Rep. Prog. Phys.* **1981**, *44*, 1–84. (b) Chatterjee, A.; Singh, A. K.; Jayaraman, A. *Phys. Rev. B* **1972**, *6*, 2285–2291. (c) Xiao, W. S.; Tan, D. Y.; Xiong, X. L.; Liu, J.; Xu, J. A. *Proc. Natl. Acad. Sci. U. S. A.* **2010**, *107*, 14026–14029.
- (27) (a) Polian, A.; Gauthier, M.; Souza, S. M.; Trichês, D. M.; Cardoso De Lima, J. C.; Grandi, T. A. *Phys. Rev. B: Condens. Matter Mater. Phys.* **2011**, *83*, 113106. (b) Nakayama, A.; Einaga, M.; Tanabe, Y.; Nakano, S.; Ishikawa, F.; Yamada, Y. *High Pressure Res.* **2009**, *29*, 245–249. (c) Gomis, O.; Vilaplana, R.; Manjón, F. J.; Rodríguez-Hernández, P.; Pérez-González, E.; Muñoz, A.; Kucek, V.; Drasar, C. *Phys. Rev. B: Condens. Matter Mater. Phys.* **2011**, *84*, 174305. (d) Souza, S. M.; Poffo, C. M.; Triches, D. M.; De Lima, J. C.; Grandi, T. A.; Polian, A.; Gauthier, M. *Physica B* **2012**, *407*, 3781–3789.
- (28) (a) Zhao, J. G.; Wang, L. H.; Dong, D. W.; Liu, Z. G.; Liu, H. Z.; Chen, G. F.; Wu, D.; Luo, J. L.; Wang, N. L.; Yu, Y.; Jin, C. Q.; Guo, Q. Z. *J. Am. Chem. Soc.* **2008**, *130*, 13828–13829. (b) Kreyssig, A.; Green, M. A.; Lee, Y.; Samolyuk, G. D.; Zajdel, P.; Lynn, J. W.; Bud'ko, S. L.; Torikachvili, M. S.; Ni, N.; Nandi, S.; Leão, J. B.; Poulton, S. J.; Argyriou, D. N.; Harmon, B. N.; McQueeney, R. J.; Canfield, P. C.; Goldman, A. I. *Phys. Rev. B: Condens. Matter Mater. Phys.* **2008**, *78*, 184517. (c) Uhoya, W.; Tsoi, G.; Vohra, Y. K.; McGuire, M. A.; Sefat, A. S.; Sales, B. C.; Mandrus, D.; Weir, S. T. *J. Phys.: Condens. Matter* **2010**, *22*, 292202.
- (29) Guñka, P. A.; Dranka, M.; Hanfland, M.; Dziubek, K. F.; Katrusiak, A.; Zachara, J. *Cryst. Growth Des.* **2015**, *15*, 3950–3954.
- (30) (a) Szotek, Z.; Temmerman, W. M.; Winter, H. *Phys. Rev. Lett.* **1994**, *72*, 1244–1247. (b) Ibarra-Hernández, W.; Verstraete, M. J.; Raty, J.-Y. *Phys. Rev. B: Condens. Matter Mater. Phys.* **2014**, *90*, 245204. (c) Mandal, S.; Cohen, R. E.; Haule, K. *Phys. Rev. B: Condens. Matter Mater. Phys.* **2014**, *90*, 060501.
- (31) (a) Slater, J. C. *J. Chem. Phys.* **1964**, *41*, 3199–3204. (b) Shannon, R. D. *Acta Crystallogr., Sect. A: Cryst. Phys., Diffr., Theor. Gen. Crystallogr.* **1976**, *32*, 751–767.
- (32) (a) Degtyareva, O.; McMahon, M. I.; Nelmes, R. J. *High Pressure Res.* **2004**, *24*, 319–356. (b) Greene, R. G.; Luo, H.; Ruoff, A. L. *Phys. Rev. B: Condens. Matter Mater. Phys.* **1995**, *51*, 597–600. (c) Aoki, K.; Fujiwara, S.; Kusakabe, M. *Solid State Commun.* **1983**, *45*, 161–163. (d) Schaufelberger, P.; Merx, H.; Contre, M. *High Temp. High Pres* **1973**, *5*, 221–230. (e) Parthasarathy, G.; Holzapfel, W. B. *Phys. Rev. B: Condens. Matter Mater. Phys.* **1988**, *37*, 8499–8501. (f) Akahama, Y.; Kobayashi, M.; Kawamura, H. *Jpn. J. Appl. Phys.* **1992**, *31*, L1621–L1624.
- (33) (a) Sakai, N.; Fritzsche, H. *Phys. Rev. B* **1977**, *15*, 973–978. (b) Tonkov, E. Yu. *Compounds and Alloys Under High Pressure: A Handbook*; CRC Press: Boca Raton, FL, 1998.